VERSITA

Central European Journal of **Physics**

Acoustically driven charge separation in semiconductor heterostructures sensed by optical spectroscopy techniques*

Research Article

Vasyl Kuryliuk[†], Artem Podolian[‡], Oleg Korotchenkov[§]

Faculty of Physics, Taras Shevchenko Kyiv National University, 01601 Kyiv, Ukraine

Abstract: We demonstrate a method of using a two-layer sandwich structure, which includes a $LiNbO_3$ plate and a semiconductor heterostructure to create an inhomogeneous stress and piezoelectric harmonic potential in the semiconductor. Both the GaAs/AlGaAs quantum well (QW) structures and SiGe/Si heterostructures are attempted, working with and without using a piezoelectric field in the semiconductor layer. The standing-wave fields generated in the semiconductor and the electron and hole distributions driven by the piezoelectric field are computed by finite element method (FEM) techniques. It is experimentally shown that, in a GaAs/Al_xGa$_{1-x}$As asymmetric double quantum well structure, the resonance enhancement of the narrower QW photoluminescence band is observed, which may be explained by the resonant charge transfer between the wider and narrower QWs. It is also shown that the piezoelectric fields quench the pure LO-phonon lines in the Raman spectra, whereas the coupled LO-phonon-plasmon mode strengthens. Experimental results indicate that the charge separation occurs in the plane of the QWs due to the piezoelectric fields. The recombination of carriers in the SiGe/Si heterostructures can be effectively enhanced by the presence of ultrasonic stress, displaying features consistent with varying electrical activity at dislocations.

PACS (2008): 78.67.De, 78.20.Hp, 62.65.+k

Keywords: ultrasonic vibrations • charge transfer • heterostructures

1. Introduction

A growing body of research data shows that the separation of charges is of major importance in a variety of physical, chemical, and biological applications [1]. Achieving charge separation and storage of optically created electron–hole pairs in semiconductor heterostructures has become an increasingly popular tool for experimental and theoretical research, and also a valuable tool for device–based tech– niques. It can be carried out in two different ways: first, as

Springer

built-in stress and electric fields achieved in conventional p–n junction and heterostructure devices [2] and quantum dot structures [3], and second, *via* an external control using inhomogeneous stress [4] or a piezoelectric field [5, 6] applied to the structures.

Here, a method of using a two–layer sandwich structure, which includes a LiNbO$_3$ plate and a semiconductor heterostructure, to create an inhomogeneous piezoelectric harmonic potential in the semiconductor is demonstrated theoretically. The standing-wave piezoelectric fields generated in the semiconductor and electron and hole distributions driven by the piezoelectric field are computed by a finite element method (FEM). The photoluminescence (PL) and Raman spectroscopy techniques are used to experimentally test the separation of charges.

2. Calculation details

2.1. Problem formulation

In this section we give a brief discussion of the generalization of the FEM method [7] to three-dimensional (3D) two–layer sandwich structure. Consider the electro–elastic vibrations of the structure, including the LiNbO$_3$ (1) and GaAs (2) parallelepiped–shaped layers shown in Fig. 1. The layers have dimensions $L_{x1}^{(\lambda)}$, $L_{x2}^{(\lambda)}$ and $L_{x3}^{(\lambda)}$, where $\lambda=$ 1, 2 is the layer number. The thickness of the bonding medium, placed between the layers, is considered to be negligibly small. The vibrations of the structure are governed by a standard set of electro–elastic equations

$$\rho_{(\lambda)}\frac{\partial^2 u_{(\lambda)i}}{\partial t^2} = -\rho_{(\lambda)}\omega^2 u_{(\lambda)i} = \frac{\partial T_{(\lambda)ij}}{\partial x_j}, \qquad (1)$$

$$T_{(\lambda)ij} = c_{(\lambda)ijkl}^E \frac{\partial u_{(\lambda)k}}{\partial x_l} + e_{(\lambda)mij}\frac{\partial \varphi_{(\lambda)}}{\partial x_m},$$

$$D_{(\lambda)n} = e_{(\lambda)nkl}\frac{\partial u_{(\lambda)k}}{\partial x_l} - \varepsilon_{(\lambda)nm}^S \frac{\partial \varphi_{(\lambda)}}{\partial x_m}, \qquad (2)$$

where ρ is the density, $\omega = 2\pi f$ is the frequency, $u_i(x_1, x_2, x_3)$ are the elastic displacement components, T_{ij} are the stress tensor components, D_i are the electric displacement vector components, $\varphi_i(x_1, x_2, x_3)$ is the electric potential, and $c_{(\lambda)}^E$, $e_{(\lambda)}$, and $\varepsilon_{(\lambda)}^S$ are the elastic stiffness tensor, piezoelectric coefficient tensor and permittivity tensor components, respectively. The indices i, j, k, l, m and n run over the Cartesian coordinates 1, 2 and 3 (x_1, x_2 and x_3). Einstein's rule of summation over repeated indices is implied. It is well known that, at a rigid interface between the layers (1) and (2), the mechanical stress and electrical fields have to satisfy the following boundary conditions:
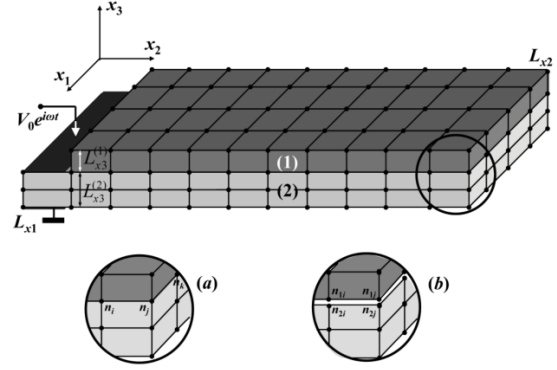
Figure 1. A simplified schematic picture of a discretized two-layer sandwich structure consisting of the semiconductor (1) and the piezoelectric LiNbO$_3$ (2) layers. In the computations, 3D-quadratic 20-node brick elements with 1496 nodes of the FEM mesh are used. A harmonic time dependence is assumed provided the vibrations are excited by an rf signal $V_0 exp(i\omega t)$, V_0 being the voltage amplitude and t the time. The discretization schemes approximating the rigid and slippery inter-layer boundary are shown in the insets a and b, respectively.

$$\begin{aligned}\varphi_{(1)} &= \varphi_{(2)}, \\ u_{(1)k} &= u_{(2)k}, \\ T_{(1)kl} &= T_{(2)kl}, \end{aligned} \qquad (3)$$

whereas the ones for the slippery boundary identifies

$$\begin{aligned}\varphi_{(1)} &= \varphi_{(2)}, \\ u_{(1)N} &= u_{(2)N}, \\ T_{(1)NN} &= T_{(2)NN}, \\ T_{(1)Nk} &= T_{(2)Nk} = 0, \end{aligned} \qquad (4)$$

where the subscript N indicates the normal component of appropriate value.

2.2. Finite-element discretization and matrix equations

Slippery and rigid types of surfaces are the two limiting cases of mechanical boundary conditions on the interface between the layers (1) and (2) in Fig. 1. Commercially available FEM software is of general purpose and often not well–suited to analysing the piezoelectric multilayered structures. Therefore, a customized FEM technique is implemented, which allows simple and very inexpensive computations of the elastic and piezoelectric fields in the resonator shown in Fig. 1.

We therefore proceed with our derivation of the correct structure discretization for the two boundary conditions by dividing the structure into small elements; see Fig. 1. Since the slippery inter-layer contact is used in experiments, this is given more detailed attention. The rigid boundary conditions are easier to implement since, in this case, the elements are continuously distributed across the x_3 axis (a in Fig. 1), so that the node points are common for all the elements at the interface (n_i, n_j, n_k). The boundary conditions for the rigid surface are then automatically satisfied. The slippery boundary conditions are attained by separating the node points for the interface elements ($n_{(\lambda)i}, n_{(\lambda)j}$ in Fig. 1b). Based on this discontinuity and on the resulting finite element mesh, the FEM matrix equation is written as

$$[K][X] - \omega^2[M][X] = [F]. \tag{5}$$

$[M]$ and $[K]$ are the mass and stiffness matrices, $[X]$ is the vector-column of u_i and φ in the node points, and $[F]$ is the vector-column of the node loads. The slippery boundary conditions (4) are taken into account by modifying the matrices in (5). First, every row and column of the matrices in (5), corresponding to the displacement vector $\overrightarrow{u}$ and the potential φ in the $n_{(1)i,j,k}$ nodes (Fig. 1,b) are supplemented by the appropriate rows and columns for the $n_{(2)i,j,k}$ nodes. Second, the above rows and columns for the $n_{(2)i,j,k}$ nodes are excluded from (5). It is worth noting that a similar procedure was performed in numerical analysis of the piezoelectric transformators [8]. We have therefore the resulting equation (5), allowing us to take the structure vibration spectrum and the spatial distributions of $u_i(x_1, x_2, x_3)$, $\varphi(x_1, x_2, x_3)$.

2.3. Charge separation in the semiconducting layer

Charge carriers confined in layer (1) of Fig. 1 are then actuated by the oscillating piezoelectric fields produced in the structure. It is assumed that the carriers are confined to a rectangular quantum well (QW) formed in layer (1) and placed in close proximity to the interface. Since the total thickness of the QW ($\approx$230 nm) and the barrier (1200 nm) layers used in experimental samples (see below) is much greater than the vibration wavelength (a few mm), we will make the conventional assumption that the components of the stress are not affected by the presence of the multilayered structure on the bottom of layer (1) in Fig. 1.

On the other hand, the electron charge density in the planes of the QWs is changed due to the generated piezo-electric fields. Noticeably, traditional semiconductor devices such as field-effect transistors, bipolar diodes and semiconductor solar cells rely heavily on electrons and holes whose motion can be described as drift and diffusion, limited by carrier recombination [9]. The drift-diffusion models, however, are not adequate to semiconductor nano-devices based, e.g., on quantum wells, since they do not take into account the quantum phenomena. On the other hand, a concise quantum mechanical simulation of the whole semiconductor device is not feasible from the numerical point of view (see, e.g., Ref. [10] and references therein). To describe semiconductor devices by quantum-mechanical modelling, Schrödinger-Poisson systems [11] are commonly utilised. The model comprises the Schrödinger operators and the Poisson equation, which accounts for the Coulomb interaction. In contrast to the drift-diffusion models, the mathematical analysis of Schrödinger-Poisson systems is less advanced. In order to describe the transport of charges in a nanoscaled semiconductor one has to consider non-equilibrium phenomena, which lead to open quantum systems [10, 12], which still awaits general techniques to set up a coupling of quantum mechanical and drift-diffusion models.

It should be stressed, however, that quantum effects most frequently take place in a localized region of a semiconductor structure, e.g., around the double barrier in a resonant tunneling device, or the active zone in a quantum well laser, whereas the rest of the structure can be well described using classical models. Therefore, the drift-diffusion models are widely applied to the in-plane motion of free charges even in a high-density regime [13]. The models have been shown to be well suited to explain the transport and recombination of electrons and holes in QWs under the piezoelectric field induced by a surface acoustic wave [14].

Following the above discussion, to study the motion of electrons (n) and holes (p) we use the drift-diffusion approximation for charge currents in the presence of an inhomogeneous piezoelectric field. Only in-plane motion of the charges is included in the present consideration. Therefore, the mechanism of charge transport can be explored within a simple model in which electrons move in the QW plane governed by the coupled drift-diffusion equations

$$\frac{\partial n}{\partial t} = -\mu_n n \Delta\varphi - \mu_n div(n\overrightarrow{\nabla}\varphi) + D_n \Delta n, \tag{6}$$

$$\frac{\partial p}{\partial t} = \mu_p p \Delta\varphi + \mu_p div(p\overrightarrow{\nabla}\varphi) + D_p \Delta p, \tag{7}$$

where $\mu_{n,p}$ are the respective mobilities, $D_{n,p}$ are the diffusion constants, and $n(x_1, x_2, t) = n_0 + n_1(x_1, x_2)exp(i\omega t)$, $p(x_1, x_2, t) = p_0 + p_1(x_1, x_2)exp(i\omega t)$ are the electron and hole densities, respectively. Here, n_0 and p_0 are the

steady-state whereas n_1 and p_1 are the bunched carrier densities. Again, FEM is employed in simulating $n(x_1, x_2, t)$ and $p(x_1, x_2, t)$ by discretizing the QW layer into small 2D elements with the surface area of S_e. Then n and p are obtained in each element through the linear sums of shape functions N:

$$n_1(x_1, x_2) = \begin{pmatrix} A_1 & A_2 & \dots & A_\eta \end{pmatrix} \begin{pmatrix} N_1(x_1, x_2) \\ N_2(x_1, x_2) \\ \vdots \\ N_\eta(x_1, x_2) \end{pmatrix}, p_1(x_1, x_2) = \begin{pmatrix} B_1 & B_2 & \dots & B_\eta \end{pmatrix} \begin{pmatrix} N_1(x_1, x_2) \\ N_2(x_1, x_2) \\ \vdots \\ N_\eta(x_1, x_2) \end{pmatrix}, \tag{8}$$

where A and B are coefficients to be determined, and η is the number of node points. The FEM matrix equations follow from (6) and (7) using the scheme of Ref. [15] and the results of Ref. [16]:

$$\begin{pmatrix} iM & -R_p \\ iM & R_p \end{pmatrix} \begin{pmatrix} A \\ B \end{pmatrix} = \begin{pmatrix} F_n \\ -F_p \end{pmatrix} \tag{9}$$

with

$$M^{\nu\nu} = \int_{S_e} \omega N_\nu N_\nu dx_1 dx_2, \tag{10}$$

$$R_{n(p)}^{\mu\nu} = \int_{S_e} (\mp D_{n(p)} + \mu_{n(p)} \varphi_\nu e^{i\omega t} N_\mu) \frac{\partial N_\nu}{\partial x_k} \frac{\partial N_\mu}{\partial x_k} dx_1 dx_2 \tag{11}$$

and

$$F_{n(p)}^{\nu} = \int_{S_e} (\mu_{n(p)} \varphi_\nu n_0(p_0) \frac{\partial N_\nu}{\partial x_k} \frac{\partial N_\mu}{\partial x_k} dx_1 dx_2, \tag{12}$$

where the upper (negative) sign in $R_{n(p)}^{\mu\nu}$ corresponds to electrons, the lower (positive) sign to holes and the summation over k=1, 2 is carried out. The material parameters used here are given in Tab. 1.

**Table 1.** Material parameters taken from Ref. [17].

Material	Symmetry	Stiffness, $10^{10}(N/m^2)$									Piezoelectric constants (C/m^2)					Relative permittivity	
		c_{11}	c_{22}	c_{33}	c_{44}	c_{55}	c_{66}	c_{12}	c_{13}	c_{14}	e_{14}	e_{15}	e_{22}	e_{31}	e_{33}	ε_{11}	ε_{33}
LiNbO$_3$	Cub. $\bar{4}3m$	20.3	20.3	24.5	6.0	6.0	7.5	5.3	7.5	0.9	0	3.7	2.5	0.2	1.3	44	29
GaAs	Trig. $3m$	11.88	11.88	11.88	5.94	5.94	5.94	5.38	5.38	0.0	-0.154	0	0	0	0	12.5	12.5

3. Experimental details

To perform the experimental measurements, an optically transparent Y- and 128° Y-cut LiNbO$_3$ and also PZT ceramic piezoelectric plates are used. The quantum well (QW) side of the GaAs/Al$_x$Ga$_{1-x}$As sample is turned to the LiNbO$_3$ plate, so that the light passing through the transparent plate is absorbed beneath the semiconductor surface exciting the free charges in the QW; see Fig. 2.

The GaAs/Al$_x$Ga$_{1-x}$As structures are grown in a V80H molecular beam epitaxy system. They consist of an n^+-type (001) GaAs substrate (substrate temperature during deposition is kept at 620–650°C), a 100-nm GaAs Si doped (10^{18-3}) buffer layer, 20 periods of an undoped GaAs/Al$_x$Ga$_{1-x}$As QW structure, and a 50-nm Al$_{0.5}$Ga$_{0.5}$As layer. A 30-nm GaAs (Be doped at a concentration of 2×10^{18} cm^{-3}) cap layer covers the structure. The QW structure itself consists of an asymmetric double QW including a narrow well (width of 5.5 nm) as the top QW, which is closer to the surface, a barrier layer of
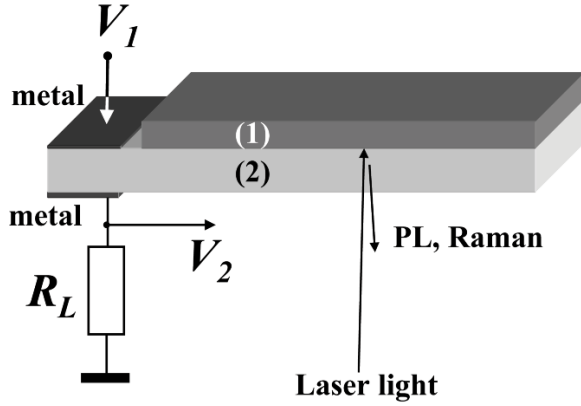
Figure 2. Schematics of the impedance setup showing a sandwich structure consisting of the semiconductor (1) and the piezoelectric LiNbO$_3$ (2) layers, metal electrodes, the load resistance R_L, the input V_1 and output V_2 voltages. Also shown are the PL and Raman scattering detection geometry.
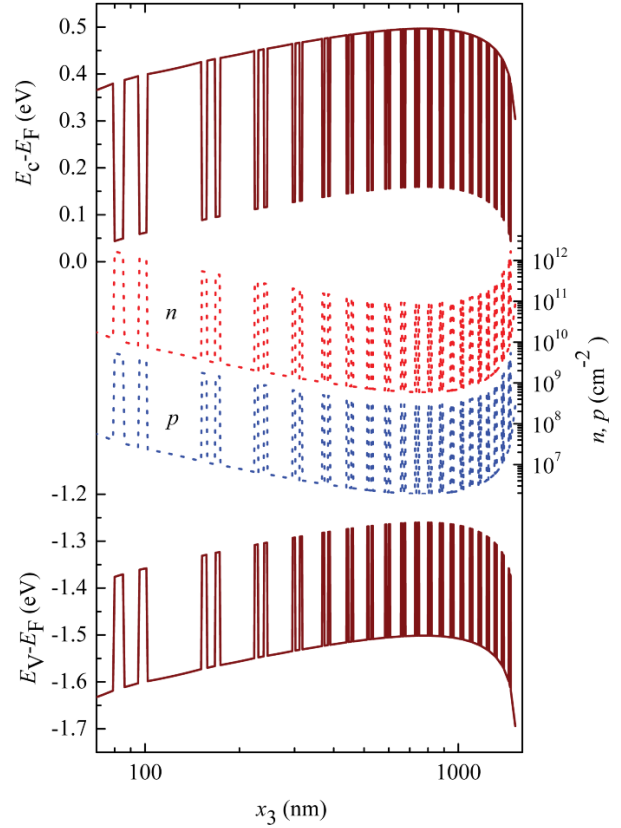

Figure 3. Computed conduction (E_C) and valence (E_V) band energy (solid), and electron and hole density (dotted) distributions in the region of 20 periods of QWs. E_F is the Fermi energy.

Al$_{0.2}$Ga$_{0.8}$As (thickness of 10 nm), and a wide well (width of 6.1 nm), separated from the next period by a 50-nm Al$_{0.5}$Ga$_{0.5}$As barrier. The growth rate is about 1000 nm per hour and the As/Ga(Al) beam equivalent pressure ratio is kept at 20-25. The quantum well layers sustain a 2DEG with a 4-K mobility of μ_n=2.0×10^6 cm^2/V·s, as obtained from the Hall measurements. Modelling the charge motion, the value of μ_n=10^6 cm^2/V·s is used. A standard value of the hole mobility (μ_p=400 cm^2/V·s) [18] is taken for the computations.

The two-dimensional electron gas density n_{2D} in the wells for the grown structure are taken by self-consistently solving the one-dimensional Schrödinger and Poisson equations [19]

$$\begin{cases} -\frac{\hbar^2}{2}\frac{\partial}{\partial x_3}\left(\frac{1}{m_e^*(x_3)}\frac{\partial}{\partial x_3}\right)\psi(x_3) + V(x_3)\psi(x_3) = E\psi(x_3), \\ \frac{\partial}{\partial x_3}\left(\varepsilon(x_3)\frac{\partial}{\partial x_3}\right)\varphi(x_3) = \frac{-e[N_D(x_3)-N_A(x_3)-n(x_3)]}{\varepsilon_0}, \end{cases}$$ (13)

where $\psi(x_3)$ is the wave function, $m_e^*(x_3)$ is the electron effective mass, $\hbar$ is the reduced Planck's constant, E is the energy, $\varepsilon(x_3)$ is the dielectric constant, e is the electron charge, $N_D(x_3)$, $N_A(x_3)$ and $n(x_3)$ are the ionized donor, acceptor and free electron concentrations, respectively, $V(x_3) = -e\varphi(x_3) + \Delta E_c(x_3)$ is the potential energy, and $\Delta E_c(x_3)$ is the conduction band offset between the Al$_x$Ga$_{1-x}$As and GaAs layers.

Following a standard method [19], we first solve the Schrödinger equation with a probe potential $V(x) = \Delta E_c(x_3)$ with $\Delta E_c(x_3)$=1.1x at 0≤ x ≤0.45 and $\Delta E_c(x_3)$=0.43+0.14x at 0.45< x ≤1 [18]. Utilising the values of $\psi(x_3)$ and E obtained and using Eqs. (5)

and (6) of Ref. [19] yields the electron density $n(x_3)$. Taking the resulting dependence $n(x_3)$, and N_D=0 at 0≤ x_3 <1462 nm (QW region) and N_D=10^{18} cm^{-3} otherwise, N_A=2×10^{18} cm^{-3} at 0≤ x_3 <30 nm (acceptor-doped cap layer), N_A=10^{16} cm^{-3} at x_3 ≥1562 nm (substrate) and N_A=0 otherwise, the potential $\varphi(x_3)$ is obtained from the Poisson equation. At this point, an improved potential $V(x_3) = -e\varphi(x_3) + \Delta E_c(x_3)$ is used and the next iteration is started yielding an improved value of $n(x_3)$. The number of iterations required to achieve an accuracy in $\varphi(x_3)$ better than 10^{-6}V is about 20. The resulting conduction band energy E_c and electron density n distributions are shown in Fig. 3, allowing us to extract the n_{2D} values used to model the charge motion in the piezoelectric fields. In the computations, the electron and hole densities in the QWs are taken to be 9×10^{11} cm^{-2} and 5×10^9 cm^{-2}, respectively.

The vibrational spectra are taken using the impedance technique [20] schematically sketched in Fig. 2. Taking the load resistance R_L to be much greater than the real part Re$\dot{Z}(f)$ of the structure's electric impedance $\dot{Z}(f)$, this

gives

$$|\dot{Y}(f)| \approx R_L^{-1} \cdot |\dot{V}_2(f)/\dot{V}_1(f)|, \qquad (14)$$

where $\dot{Y}(f) = \dot{Z}^{-1}(f)$ is the complex electrical conductivity of the sample and the voltages $\dot{V}_1(f)$ and $\dot{V}_2(f)$ are shown in Fig. 2. Then the frequency dependence $|\dot{Y}(f)|$ represents the structure's vibrational spectrum [21]. The slippery contact is utilized by freely placing a semiconductor [layer (1) in Fig. 1] onto the LiNbO$_3$ plate [layer (2)].

PL and Raman scattering are excited by 647.1–nm (Kr$^+$) and 488.0–nm (Ar$^+$) laser lines, respectively, and collected in a near–backscattering geometry perpendicular to the QW plane. The excitation energy is above the ground states in the QWs but lies below the band gap of the Al$_{0.5}$Ga$_{0.5}$As barriers. The exciting light is focused on a region of the order of 100 μm in diameter. The sample could be shifted laterally relative to the optical axis of the double SPEX monochromator used to disperse the PL and Spectra Pro 300 (Acton Research) monochromator employed in the Raman measurements. The signal from the sample is detected by employing a Hamamatsu R928 photomultiplier tube followed by a Model 162 Boxcar Averager. By changing the aperture delay, the PL detection moment can be shifted along the time scale within the period of the standing wave piezoelectric potential (experimental details are published elsewhere [6]). All measurements are performed at room temperature.

A slightly different vibration set is used to affect free carrier lifetimes in the SiGe/Si heterostructures. The sample is mounted onto the metallized piezoceramic transducer. An rf voltage drives the transducer resulting in acoustic vibrations of the SiGe/Si sample. The voltage amplitude V_0 is continuously adjustable between V_0=0 and $\approx$10 V. The strain amplitude inside the sample is then estimated by the method described above, yielding a longitudinal stress amplitude of about 100 MPa. The data presented here are obtained with a 1–μm thick Si$_{0.83}$Ge$_{0.17}$ layer grown by chemical vapor deposition with no intentional doping on a 300–μm thick (100)Si substrate. There is no graded layer introduced on the SiGe/Si interface in order to compensate for the lattice mismatch between SiGe and Si. To attain the effective lifetime of the photogenerated carriers in SiGe the photoconductivity decay (PCD) method is used. The Ohmic contacts are made from Al. The LED pulses of a 100–μs length with rise and fall times of $\leq$1.2 μs are chosen to satisfy the low–level injection conditions (the injected carrier concentration is about 1% of its steady value). Decay transients were stored in the computer memory using an analog–to–digital converter (ADC) with a resolution of $\approx$2 μs.

4. Validating the computation results

4.1. Numerical and experimental studies of vibrational spectra

This section is devoted to testing our computation scheme. Figure 4 displays the comparison of the measured (1) and computed (2) vibrational spectra of a separated piezoelectric resonator LiNbO$_3$ (a) and a two–layer LiNbO$_3$–GaAs structure with slippery (b) and rigid (c) interface contacts. The analysis reveals that the measured resonance frequencies lie well within the error bars originating from the experimental uncertainty in measuring the linear dimensions displaced in a. Shown by dotted lines in c is the modelled spectrum obtained at $L_{x2}^{(1)} = L_{x2}^{(2)}$, illustrating that, in contrast to the slippery contact (not shown here), the resonance frequencies are very sensitive to a proper account for the difference in the dimensions of layers (1) and (2) in Fig. 1.

The modelled results illustrate that, regardless of the contact type, the placement of the semiconductor layer shifts the vibrational spectrum to lower frequencies [spectra (2) in b and c compared with (2) in a]. Meanwhile, for the slippery contact [(2) in b], the frequency difference $f_{n+1} - f_n$ between the consequent (n+1)th and nth modes remains nearly the same for different n, as opposed to the rigid contact [(2) in c] exhibiting spectrum transformations with changed relative positions in the mode frequencies.

These trends are exactly the results observed experimentally; see (1) in Fig. 4. The results can be qualitatively explained using a simple model whereby the vibrations of the structure are excited by a piezoelectric LiNbO$_3$ and are accompanied by piezoelectric fields. With the slippery boundary conditions, the GaAs layer is merely a passive element causing a mass load on the LiNbO$_3$ surface. This causes the low–frequency shift of the vibrational spectrum, with no change in the relative positions of the mode frequencies. The rigid contact turns out to enlarge the linear dimensions of the vibration structure, which then causes a relative shift in the frequency spectrum lines.

4.2. Spatial distributions of the electric fields

The computed distributions of the potential (φ) and normal (E_{x3}) components of the field strength are shown in Fig. 5. They exhibit the node and antinode spatial positions in the standing wave, establishing that both the spatial positions and the values of φ and E_{x3} vary sensitively with tuning of the resonance frequency (a, c and e compared with b, d and f in Fig. 5).

When comparing the computed and experimental results,
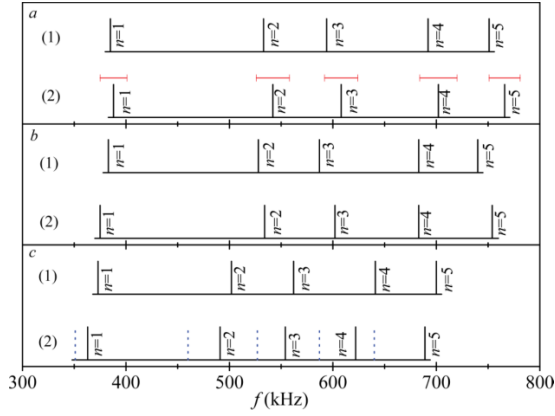
**Figure 4.** Measured (1) and computed (2) vibrational spectra of a separated piezoelectric resonator LiNbO$_3$ (a) and a two-layer Y-cut LiNbO$_3$-GaAs structure with a slippery (b) and rigid (c) interface contact. $L_{x1}^{(1)} = L_{x1}^{(2)}$=4.95 mm, $L_{x2}^{(1)}$=4.14 mm, $L_{x2}^{(2)}$=5.64 mm, $L_{x3}^{(1)} = L_{x3}^{(2)}$=0.74 mm. The dotted-line spectrum in c is computed at $L_{x2}^{(1)} = L_{x2}^{(2)}$=5.64 mm. The error bars in a are due to taking into account experimental uncertainty in measuring the linear dimensions $L_{x1}^{(2)}$, $L_{x2}^{(2)}$ and $L_{x3}^{(2)}$ and relaxing the above assumption that all the opposite layer edges are strongly parallel, which is taken to be 0.005 mm. n is the number of the vibrational mode.

there exists some ambiguity in the proper choice of boundary conditions. Indeed, even in the absence of a bonding material, coupling of the two layers (1) and (2) can exist, due to the mechanical coupling of the two sliding media through the normal component of the stress, which depends on the force that presses the sample against the plate surface. In an attempt to analyze the departure of the observed field distributions from that computed theoretically, a number of the computed and measured results are contrasted in Fig. 6. It is seen that the placement of the semiconductor layer [(2) in Fig. 1], either in a rigid (a in Fig. 6) or slippery (b) interface contact, seems to have no very sensitive effect on the φ spatial distribution in a free-standing LiNbO$_3$ plate displayed in c. The latter in turn is reproduced in experiments fairly well. Also illustrated in Fig. 4(2) and Fig. 6(a, b) is the fact that, having to deal experimentally with $L_{x2}^{(1)} < L_{x2}^{(2)}$, one should account for this difference in modelling the vibrational spectrum of the rigidly bonded layers (dotted- and solid-line spectra in c of Fig. 4). However, this has no profound effect on the shape of the potential distributions (a and b in Fig. 6).
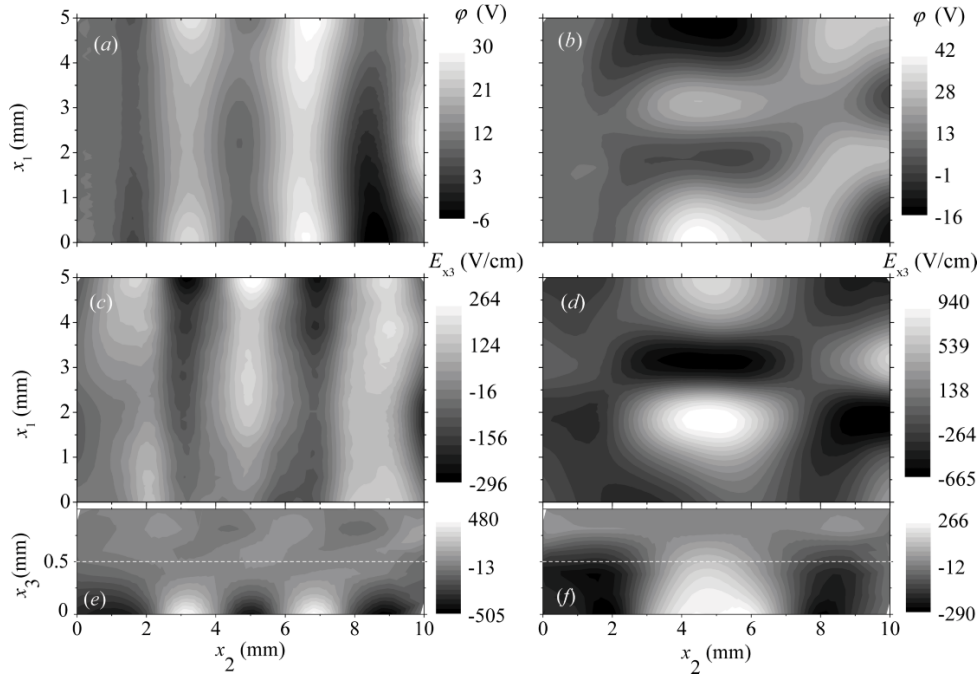
Figure 5. Computed distributions of the piezoelectric potential φ (a, b) and E_{x3} component (c-f) at the rigid interface of a two-layer 128° Y-cut LiNbO$_3$-GaAs structure (a-d) and in the middle cross-section x_2x_3 (e, f) at the n=3 (a, c, e) and n=6 (b, d, f) resonance vibrational modes. The linear dimensions are $L_{x1}^{(1,2)}$=3.75 mm, $L_{x2}^{(1,2)}$=13.8 mm, $L_{x3}^{(1,2)}$=0.78 mm. The interface is indicated by dashed lines in e and f. Applied voltage V_0=10 V.
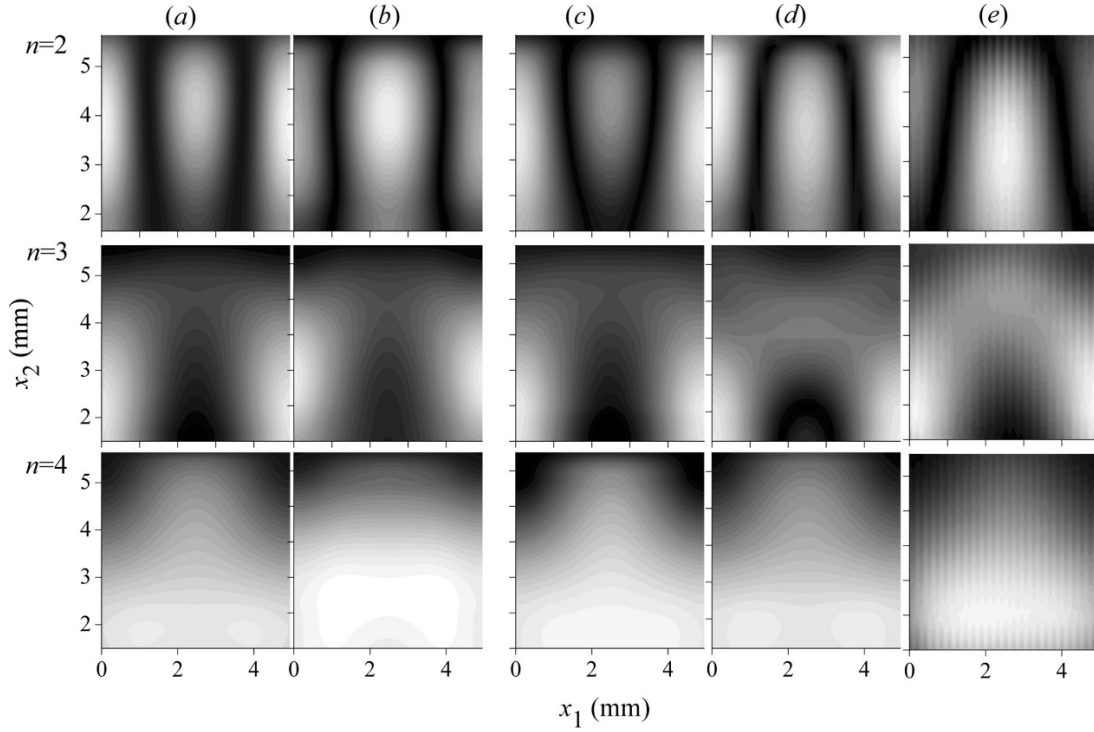
Figure 6. Computed (a-d) and measured (e) distributions of the piezoelectric potential φ in a two-layer Y-cut LiNbO$_3$-GaAs structure with a rigid (a and b) and slippery (c) interface contact and at the surface of the free-standing LiNbO$_3$ plate (d, e). n is the number of the vibrational mode. The linear dimensions are indicated in the caption of Fig. 4, and a corresponds to $L_{x2}^{(1)}$=4.14 mm, $L_{x2}^{(2)}$=5.64 mm, whereas b and c - to $L_{x2}^{(1)} = L_{x2}^{(2)}$=5.64 mm. The φ measurement setup was previously discussed [28].

As a final note, Fig. 7 shows the computed free electron (c) and hole (b) densities in the QW plane, compared with the φ distribution. As expected, the mobile electrons and holes follow the piezoelectric potential variations, so that the electrons are collected at the antinodes of φ (white areas in a) whereas the holes are gathered just in the node regions (black areas in a).

Since the lifetime of the photoexcited electron–hole pairs is much less then the acoustic wave period, at a given time moment t, the radiative recombination features are sensitive to the electron gas density achieved at a PL detection point. This density in turn is sensitive to φ, allowing us to engineer the spatially and temporally distributed depleted and accumulated charge regions formed in the plane of the QW and to tune the plasma–exciton recombination processes both spatially and temporally, as discussed previously [6]. In this work, room–temperature PL is attempted to test for free charge transfer between the near QW layers occurring due to the E_{x3} component of the piezoelectric field.

Therefore, having validated the capabilities of the computation techniques, we proceed to study the charge sepa-

ration in the acoustic fields.

5. Acoustically driven charge separation in semiconductors

5.1. Resolving photoluminescence

The PL spectrum exhibits a broad emission arising in the overlapping wide and narrow QWs (W and N in Fig. 8). The PL excitation and detection point is placed just in the antinode region of E_{x3} (cf. white area in Fig. 5d), which is detected by the node area of φ (black area in Fig. 5b) sensed on the surface of a free–standing LiNbO$_3$ plate.

The data of Fig. 8 display variation of the PL spectrum with increasing piezoelectric field component perpendicular to the QW plane specified in terms of the applied voltage amplitude V_0. Increasing the normal component makes the lines even broader and shifts them to a lower energy, which may in part be due to the quantum–confined Stark effect [22], and in part originate from the varying electron density in the oscillating piezoelectric field at
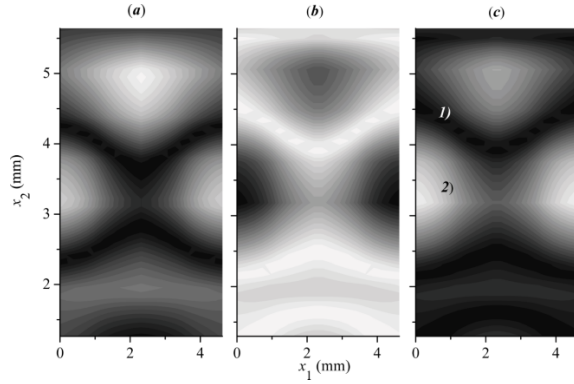
Figure 7. Computed distribution of the piezoelectric potential (*a*) and the free hole (*b*) and electron (*c*) densities in the QW plane of a two-layer Y-cut LiNbO$_3$-GaAs structure. White and black regions correspond to maximum and minimum values, respectively, of φ and charge densities. Taking V_0=100 V, these values for n_{2D} are found to be 2.4×10^{12} and 0.2×10^{12} cm^{-2}, respectively. Points labelled 1) and 2) are used to explain the Raman spectra variations.
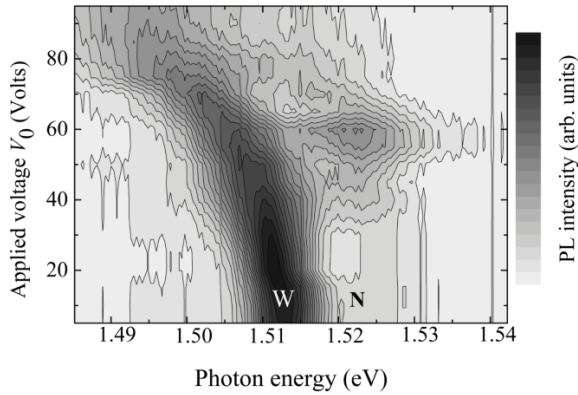
Figure 8. Gray-scale representation of the PL spectrum *versus* normal component of the piezoelectric field strength E_{x3} specified in terms of the applied voltage amplitude V_0 showing a resonance enhancement of the narrow well emission line. The spectra are taken at the moments of peak values of E_{x3}. The n=6 vibrational mode is employed.

the detection point of the PL.

Also seen is the resonance enhancement of the narrow QW emission band (darkened N band at V_0 ranging from ≈50 to ≈65 V in Fig. 8). Based on the available mechanisms of charge transfer in cascade systems with QWs, the observed enhancement can be explained by the overbarrier excitation of charge carriers [23, 24] and by the tunnelling of charges [25, 26] from the wider to the narrower wells. Modelling of the resonant charge transfer in the structure is most clearly exemplified in Fig. 9 exhibiting energy level alignment in the absence of the piezoelectric field (*a*) and in the presence of E_{x3} (*b*).
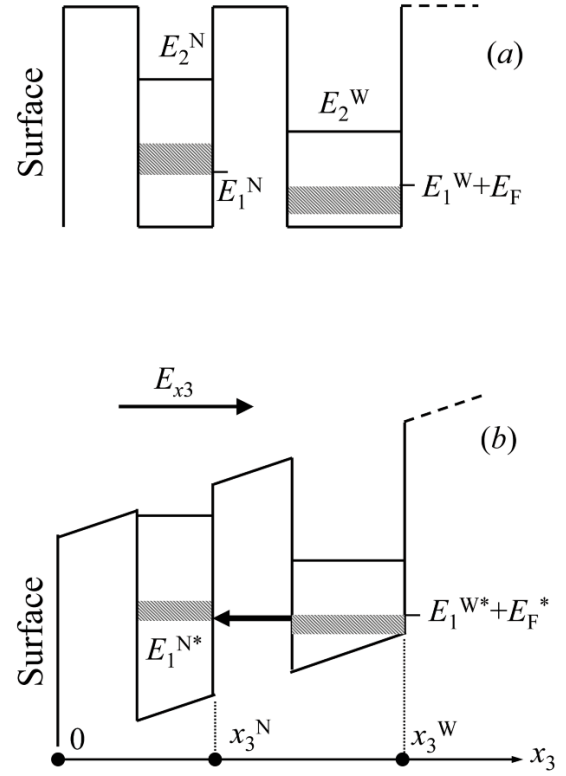
Figure 9. The band alignment in the structure, in the absence of the piezoelectric field (*a*) and in the presence of E_{x3} (*b*) The E_F band width depends upon φ due to the variation in n_{2D}. The electron energy levels are $E_1^{N*} = E_1^N + eE_{x3}x_3^N$ and $E_1^{W*} = E_1^W + eE_{x3}x_3^W$. Arrow indicates the tunnelling transport of free electrons.

For a degenerate electron gas in the wells, the Fermi energy band E_F is [27]

$$E_F = \frac{\pi \hbar^2 n_{2D}}{m_e^*},\qquad(15)$$

where m_e^*=0.067m_0 [18] and m_0 is the free-electron mass. Taking n_{2D}=10^{11} cm^{-2} in the φ node region yields $E_F^* \approx$ 3 meV. Then the resonant tunnelling occurs if

$$E_1^N + eE_{x3}x_3^N = E_1^W + eE_{x3}x_3^W + E_F^*.\qquad(16)$$

This gives the normal field estimate E_{x3}=1.6×10^4 V/ cm at E_1^N=54 meV, E_1^W=82.5 meV, $x_3^N \approx$56 nm and $x_3^W \approx$72 nm, which indeed occurs in the experimental structure, thus demonstrating the feasibility of the suggested mechanism.

5.2. Affecting LO-phonon coupled modes in Raman spectra

For better understanding of the in-plane charge separation (*b* and *c* in Fig. 7), the Raman spectroscopy tech–
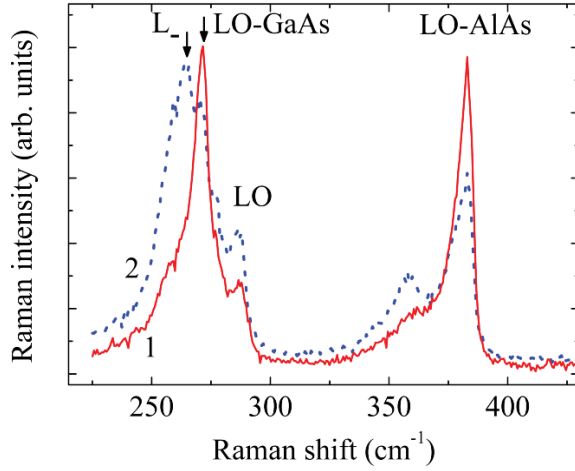
Figure 10. Raman spectra of GaAs/AlGaAs in the back-scattering geometry taken in points 1 and 2 in Fig. 7c (spectra 1 and 2, respectively). The peak labelled LO is the LO phonon arising from the GaAs wells. LO-GaAs and LO-AlAs are the GaAs- and AlAs-like modes of the LO phonons in AlGaAs barrier layers. The arrow L_- represents one of the coupled LO-phonon-plasmon modes.

nique is employed. Raman scattering strongly depends on lattice excitations and longitudinal optical phonons which couple strongly with collective oscillations of plasmons [29]. It has previously been observed that the coupled modes of LO-phonons and plasmons, observed in the Raman spectra, can be frequency-tuned by changing the 2DEG density [30]. This is due to the ability to generate dense electron population optically under a c.w. laser light serving as a signal beam. Here we expect that acoustically varying n_{2D} can affect the Raman spectra in our samples.

Raman spectra 1 and 2 shown in Fig. 10 are taken in points of depleted (point 1 in Fig. 7c) and accumulated (point 2) electron densities, respectively, which, again, are detected by sensing the node and antinode areas of φ, respectively (cf. Fig. 7a). They contain two prominent sets of strong peaks related to pure LO-phonons in GaAs and AlAs [31]. Comparing with the well-known GaAs- and AlAs-like vibrational modes [18], the peaks labelled LO-GaAs and LO-AlAs are assigned to LO vibrational modes of the Ga–As and Al–As bonds, respectively, in the AlGaAs layers, whereas the one marked LO is related to LO vibrational modes of the Ga–As bond in GaAs QWs. Obviously, weak peaks located at lower frequencies compared to that of LO phonons may be related to the TO phonons of GaAs and AlAs-like in AlGaAs alloy [32], and also to coupled LO-phonon-plasmon modes [33].

Most noticeably, the coupled LO-phonon-plasmon mode L_- strengthens remarkably in spectrum 2 with enhance-

ment of the free electron density (point 2 in Fig. 7c). A careful examination also shows that the peak position of the L_- line gradually shifts to lower frequency within ≈ 5 cm^{-1} with increasing n_{2D} due to either lateral shifting of the detection point or gradually increasing the piezoelectric field strength.

Bearing in mind the collective behavior of the interacting electron gas in semiconductors [34], one would expect the changes in the Raman spectra observed in the driving piezoelectric field. Note that in polar lattices like GaAs, the LO mode involves a polarization oscillation which interacts dynamically with the free carriers *via* the long-range Fröhlich interaction. The ion oscillations are accompanied by an electron cloud, which screens the polarization field created by the lattice. The behavior of the electron gas exhibiting the long-range Coulomb interaction includes screening and collective excitation effects. The collective charge excitations, plasmon modes, interact dynamically with the LO phonons. At low electron densities (e.g., the ones achieved in point 1 of Fig. 7c), the coupling can be neglected. The L_- mode is then negligibly small and can barely be distinguished on the low-frequency side of the LO-phonon line in spectrum 1 of Fig. 10. In the opposite limit, at high enough density of n_{2D}, the interaction can be approximated by the static screening, *i.e.*, the free carriers instantly screen the electric field generated by the ion displacement, and the LO phonon recovers the nonpolar energy of the TO mode. Approach to this limit is manifested in the low-frequency shift of L_- in increased piezoelectric fields. In the intermediate case (e.g., in point 2 of Fig. 7c), a dynamical coupling of the two modes occurs, giving rise to the coupled modes.

More quantitatively, the frequency shift of the coupled L_- mode with varying n_{2D} has been modelled by the method of Ref. [34], exhibiting a fairly good agreement of the observed and estimated results.

Figure 10 also demonstrates the ability of the varying free carrier density to screen the ionic character of the LO phonon. The LO-GaAs and LO-AlAs lines appear to be quenched in spectrum 2, although this is unlikely to occur with the LO line. The quenching itself may be of further interest due to the fact that the screening can affect the relaxation of photogenerated carriers through coupling effects which can adversely affect the spectrum of diode lasers and the performance of semiconductor electronic devices [36].

5.3. Tuning the carrier lifetimes in SiGe layers

In an attempt to explore the mechanical stress accompanying the vibrations, the photocurrent transients are taken in the SiGe/Si heterostructures subject to the stress field.
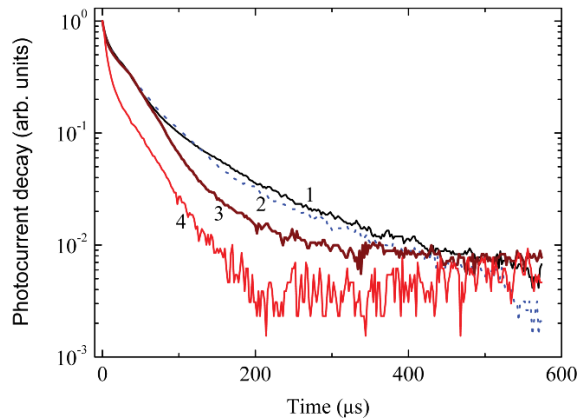
Figure 11. Representative PCD transients for $Si_{0.83}Ge_{0.17}$/Si heterostructure taken at V_0=0 (1), 2.5 (2), 5 (3) and 7.5 (4) Volts. The vibration frequency is 6.8 MHz.

Typical PCD transients are shown in Fig. 11. Application of ultrasonic stresses produces a decrease in the carrier lifetime, evidenced by accelerated decays, as illustrated by comparing curves 2-4 with curve 1. The lifetime is recovered with a timescale of a few tens of seconds to almost 100% of the initial value.

In explaining this effect, many potentially relevant factors (including thermal effects of ultrasound, mechanical actuation of interface and surface roughness, varying defect concentrations in acoustic fields, electrode uniformity over the course of measurements, *etc.*) and their effects on the measured photocurrents are to be systematically controlled, prescribed and quantified. The treatment of these effects, which warrants careful future study, is beyond the scope of this work. Here we note that the data are seemingly consistent in several aspects with dislocation involvement, which has been found so far to be the most important parameter in stress-induced engineering of electronic parameters in semiconductors [37].

High densities of misfit dislocations are present in the heterostructures to relieve the Si and Ge lattice mismatch strain. It has been shown that the threading arms accompanying the misfit segments are detrimental for devices and therefore must be minimized [38]. It has also been suggested that partial dislocations are of importance, controlling the mechanical and electronic properties of Si and SiGe since the atomic reconstruction occurs at the dislocation core, eliminating dangling bonds and thus making the dislocation electrically inactive [39].

It is therefore straightforward to assume that the dislocation core defects or impurity atoms, which have segregated at the dislocations, are released from them in acoustic fields thus increasing the number of dangling bonds, which become electrically active. As a consequence, the recom-

bination of carriers captured at dislocation bands can be enhanced. This in turn shortens the PCD observed in Fig. 11. These defects can furthermore exchange electrons and holes near the surface and interface, and this may account for why we measured an inverse photovoltage in the spectral range between the Si and Ge bandgap energies induced by the ultrasonic stress (not shown here). This observation opens up the new possibility of engineering electronic properties of SiGe layers.

6. Conclusions

In summary, we have addressed the piezoelectric and stress fields arising in $LiNbO_3$–GaAs and piezoceramic-SiGe acoustic resonance structures and designed to engineer optical and electronic properties of GaAs and SiGe heterostructures. Computationally, particular emphasis has been given to piezoelectric field distributions by employing FEM techniques. Experimentally, a GaAs/Al_xGa_{1-x}As asymmetric double quantum well structure subject to the piezoelectric field has been studied by photoluminescence and Raman scattering techniques. The resonance enhancement of the narrower QW PL band has been observed, consistent with a picture of the resonant charge transfer between the wider and narrower QWs. The quenching of the pure LO-phonon lines seen in the Raman spectra has been accompanied by the strengthening of the coupled LO-phonon-plasmon mode, indicative of charge separation in the plane of the QWs caused by the piezoelectric fields. The photocurrent and photovoltage parameters of SiGe layers can dynamically be affected by the stress fields developed in the vibrating structures.

Acknowledgments

References

[1] C. H. Hamann, W. Vielstich, Electrochemistry (Wiley-VCH, Weinheim, 1998)

[2] S. M. Sze, Physics of Semiconductor Devices, 2nd edition (Wiley, New York, 1981)

[3] P. Boucaud, S. Sauvage, C. R. Phys. 4, 1133 (2003)

[4] R. B. Balili, D. W. Snoke, L. Pfeiffer, K. West, Appl. Phys. Lett. 88, 031110 (2006)

[5] C. Rocke et al., Phys. Rev. Lett. 78, 4099 (1997)

[6] O. A. Korotchenkov, A. Cantarero, Phys. Rev. B. 75, 085320 (2007)

[7] T. Makkonen, A. Holappa, J. Ella, M. M. Salomaa, IEEE T. Ultrason. Ferr. 48, 1241 (2001)

[8] N. F. Shulga, A. M. Bolkisev, Vibration of piezoelectric bodies (Naukova dumka, Kyiv, 1990) (in Ukrainian)

[9] S. Selberherr, Analysis and Simulation of Semiconductor Devices (Springer, Vienna, 1984)

[10] H.-C. Kaiser, J. Rehberg, Nonlinear Anal.-Theor. 41, 33 (2000)

[11] E. Kapon, Semiconductor Lasers. Fundamentals (Academic Press, San Diego, 1999)

[12] N. G. Einspruch, W. R. Frensley (Eds.), Heterostructures and Quantum Devices (Academic Press, San Diego, 1994)

[13] R. Rapaport et al., Phys. Rev. Lett. 92, 117405 (2004)

[14] A. García-Cristóbal, A. Cantarero, F. Alsina, P. V. Santos, Phys. Rev. B. 69, 205301 (2004)

[15] O. C. Zienkiewich, The Finite Element Method in Engineering Science (McGraw-Hill, London, 1971)

[16] O. A. Korotchenkov, O. I. Polovina, V. V. Kurylyuk, IEEE T. Ultrason. Ferr. 54, 2529 (2007)

[17] B. A. Auld, Acoustic Fields and Waves in Solids, Vol. 1 (Wiley, New York, 1973)

[18] S. Adachi, J. Appl. Phys. 58, R1 (1985)

[19] I.-H. Tan, G. L. Snider, L. D. Chang, E. L. Hu, J. Appl. Phys. 68, 4071 (1990)

[20] D. A. Berlincourt, D. R. Curran, H. Jaffe, In: W. P. Mason (Ed.), Physical Acoustic, Vol. 1, part. A (Academic Press, New York, 1964)

[21] X.-H. Du, Q.-M. Wang, K. Uchino, IEEE T. Ultrason. Ferr. 50, 312 (2003)

[22] D. A. B. Miller et al., Phys. Rev. B 32, 1043 (1985)

[23] N. Peyghambarian, S. W. Koch, A. Mysyrowicz, Introduction to Semiconductor Optics (Prentice Hall, Englewood Cliffs, 1993)

[24] C. Gmachl et al., Rep. Prog. Phys. 64, 533 (2001)

[25] S. Tarucha, K. Ploog, Phys. Rev. B 39, 5353 (1989)

[26] T. Ohtsuka et al., J. Appl. Phys. 94, 2192 (2003)

[27] A. Ya. Shik, L. G. Bakueva, S. F. Musikhin, Physics of Low-Dimensional Systems (Nauka, St. Petersburg, 2001) (in Russian)

[28] A. B. Nadtochii, O. A. Korotchenkov, H. G. Grimmeiss, Phys. Rev. B 67 125301 (2003)

[29] T. Yuasa I. et al., Phys. Rev. B. 33, 1222 (1986)

[30] B. Fluegel, A. Mascarenhas, D. W. Snoke, L. N. Pfeiffer, K. West, Nat. Photonics. 1, 701 (2007)

[31] A. S. Barker Jr., A. J. Sievers, Rev. Mod. Phys. 47, S1 (1975)

[32] O. K. Kim, W. G. Spitzer, J. Appl. Phys. 50, 4362 (1979)

[33] T. Yuasa et al., Appl. Phys. Lett. 46, 176 (1985)

[34] P. Y. Yu, M. Cardona, Fundamentals of Semiconductors, Physics and Material Properties (Springer, Berlin, 1999)

[35] P. Giudici, A. R. Goñi, C. Thomsen, K. Eberl, M. Hauser. Phys. Rev. B 73, 045315 (2006)

[36] E. M. Conwell, Solid State Physics (Academic, New York, 1967)

[37] I. V. Ostrovskii, O. A. Korotchenkov, T. Goto, H. G. Grimmeiss, Phys. Rep. 311, 1 (1999)

[38] P. M. Mooney, J. O. Chu, Annu. Rev. Mater. Sci. 30, 335 (2000)

[39] J. R. Chelikowsky, Phys. Rev. Lett. 49, 1569 (1982)